Iranian Journal of Fuzzy Systems

Volume 22, Number 1, (2025), pp. 147-168

Original paper

Hybrid neuro-fuzzy integral sliding mode control technique optimized UPQC for power quality improvement in solar systems

L. Saihi [1] and B. Berbaoui [2]

[1] *Unité de Recherche en Energies Renouvelables en Milieu Saharien URERMS, Centre de Développement des Energies Renouvelables CDER, BP. 478, 01000 Adrar, Algeria*

[2] *Laboratory of Sustainable Development and Informatics, Department of Electrical Engineering, University of Ahmed Draia Adrar, 01000 Adrar, Algeria.*

saihi_lakhdar@urerms.dz, berbaoui.brahim@univ-adrar.edu.dz

Abstract

This paper presents the design and evaluation of a Photovoltaic-Unified Power Quality Conditioner (PV-UPQC) with series and shunt compensators connected via a DC link. The shunt compensator extracts power from the PV array, compensates harmonic currents and reactive power, and operates at the maximum power point (MPP) under real solar conditions in Adrar, Algeria. Hybrid Neuro-Fuzzy (HNF) integrated with Integral Sliding Mode Control (ISM-C) address chattering issues, improving energy extraction and power quality under variable conditions. Grey Wolf Optimizer (GWO) tunes controller (HNF-ISM-C) parameters, with simulations demonstrating the superiority of HNF-ISM-C over conventional methods. The proposed system significantly enhances power quality, especially under fluctuating irradiation and temperature conditions. The results highlight the robustness and effectiveness of the optimized control strategy in real-world applications.

Keywords: UPQC, ShAPF. Photovoltaic system, HNF-integral sliding mode control, GWO.

1 Introduction

The increasing integration of environmentally friendly renewable energy systems, particularly solar PV energy and wind energy, into modern distribution systems is driven by environmental considerations. However, the intermittent nature of these energy sources presents challenges [8]. Modern distribution systems are characterized by the prevalence of power electronics-based loads, which exhibit high nonlinearity. The upsurge in installations of renewable energy sources and nonlinear loads contributes to various power quality issues at both the load side and grid side [30].

Renewable energy sources, like solar PV energy, introduce intermittency into distribution systems, giving rise to voltage quality issues such as sags/swells, interruptions, flicker, and grid instability [8]. These problems can lead to frequent false tripping of power electronic systems, malfunctions, false triggering of electronic systems, and increased heating of capacitor banks [1, 30]. Quality concerns with current primarily emerge from the nonlinear loads connected in distribution systems. These loads inject harmonics into the distribution system, causing distortion of the point of coupling (PCC) voltage, especially in weak grids, resulting in losses in distribution cables and transformers [1].

To tackle these challenges, custom power devices such as the Distribution Static Compensator (DSTATCOM), Dynamic Voltage Restorer (DVR), and Unified Power Quality Conditioner (UPQC) are employed [14]. DSTATCOM, a shunt-connected power electronic system, compensates for power quality issues caused by loads, including reactive current, harmonics, and load imbalance. DVR, a series-connected power electronic system, addresses grid voltage sag/swell issues [19]. The UPQC, comprising back-to-back connected shunt and series compensators, integrates the functionalities of both DSTATCOM and DVR [8].

Corresponding Author: L. Saihi

Received: July 2024; Revised: January 2025; Accepted: February 2025.

https://doi.org/10.22111/ijfs.2025.49224.8678

In recent developments in control systems, various advanced nonlinear techniques have emerged to effectively manage PV solar systems integrated with UPQC to mitigate harmonic currents and reactive power. Sliding mode control (SM-C), as discussed in [2, 5, 6, 7, 20], stands out as a sophisticated methodology tailored for controlling nonlinear systems. Its primary goal is to guide the controlled dynamics of the system toward a designated sliding surface, maintaining it until equilibrium is achieved. Several research studies have demonstrated the practical application and effectiveness of SM-C. In [7], two distinct strategies were presented: the conventional PI controller and the SM-C of a three-phase ShAPF, with a subsequent comparison of these approaches. Additionally, in [2], a comparative study involving simulation and experimentation was introduced, evaluating the SM-C against a PI regulator in the context of controlling the DC bus voltage of a three-phase ShAPF.

In [20], the aim was to introduce a vector operation technique for governing three-phase converters using one-cycle control. This paper outlines a comprehensive large-signal model for a three-phase APF, incorporating the vector operation technique within an innovative coordinate system. The study further encompasses the development of SM-C within these coordinates, coupled with a modulator to generate control signals in the natural frame. In [5], a novel approach is presented, introducing an adaptive dynamic special global SM-C for a three-phase APF. This controller utilizes a proportional integral derivative (PID) sliding surface and incorporates a radial basis function (RBF) neural network. The global PID sliding manifold enhances robustness, reduces steady-state errors, and includes a nested dynamic SM-C to minimize chattering effects. To tackle parameter uncertainties and external disturbances, an RBF neural estimator is integrated, contributing to overall system performance improvement. In [6], continuous terminal sliding mode control is introduced, utilizing a meta-cognitive fuzzy neural network for an APF. Diverging from conventional strategies, this approach ensures high-performance current control with an integral-type terminal sliding surface, aiming to minimize tracking errors within a finite time. However, SM-C is known for its ripple effects, arising from the discontinuous nature of the control's switching functions. These ripple effects can negatively impact power quality and introduce additional harmonics. To overcome this challenge and enhance the performance of classical SM-C, an alternative robust strategy can be considered.

This study proposes methods to address ripple issues by replacing the discontinuous component with artificial intelligence techniques like fuzzy logic control (FLC) or artificial neural networks (ANN). However, traditional fuzzy logic systems require expert knowledge to define rules, and tuning membership function parameters can be challenging and time-consuming, leading to potential errors in obtaining the desired response. Moreover, if training data is insufficient, relying solely on artificial neural networks may not cover all operating states. To overcome these challenges and leverage the advantages of both systems while compensating for their drawbacks, the hybrid neuro-fuzzy (HNF) is introduced. HNF combines the learning capabilities of artificial neural networks with the inference capabilities of rule-based fuzzy logic control, providing a comprehensive solution under the supervision of learning capabilities. This hybrid approach is employed to mitigate chattering effects and enhance power quality, gaining prominence in control strategies. In this study, a hybrid strategy, HNF-ISM-C, is implemented for a three-phase ShAPF, demonstrating its effectiveness in mitigating ripple effects and introducing a more advanced and intelligent control approach through the utilization of artificial neural networks.

The central challenge in implementing HNF-ISM-C lies in determining its optimal parameters. A prior investigation [15] explored an optimal design approach for ShAPF using the particle swarm optimization (PSO) algorithm, showcasing improved performance. This study delves into the application of PSO to optimize the PI controller for ShAPF's DC link voltage, leveraging the PSO tuning method for its rapid convergence. To address PSO's limitations, the study proposes the grey wolf optimizer (GWO) tuning approach for the SM controller based on the HNF algorithm. The suggested GWO tuning method offers a balanced blend of exploration and exploitation, adept at avoiding local optima. It is user-friendly, reliable, and applicable to complex optimization challenges, with the overarching goal of enhancing the efficiency of PV solar systems using UPQC and reducing output fluctuations of the proposed controller.

The research is structured into five sections. The first section outlines the mathematical model of the PV-UPQC system configuration, presenting a three-phase structure integrating a PV system through a shared DC link. It incorporates a shunt active power filter (ShAPF) connected in parallel with the AC grid and a series active power filter (SeAPF) connected in series with the grid. The second section focuses on Harmonic Extraction and Estimation using the instantaneous active and reactive power theory (P-Q theory), addressing harmonics and reactive power demands from nonlinear loads in the three-phase ShAPF. The third section, Controller Synthesis, details the process involving the cascading of two loops to ensure voltage control on the DC side of the ShAPF. Additionally, it introduces the robust modified SM-C for the PV solar system under varying irradiation, discussing the integration of this control strategy to enhance system performance. In the fourth section, Integration of HNF explores the incorporation of HNF to replace the switching functions of conventional SM-C. This strategic integration aims to mitigate ripple effects and enhance the overall system performance. The fifth section introduces the Grey Wolf Optimizer (GWO) Algorithm for Parameter Optimization, playing a crucial role in optimizing the parameters of the HNF-ISM-C controller. Subsequently, numerical results are presented, validating the robustness and performance of the HNF-ISM-C using GWO for ShAPF under various conditions. The final section concludes the study, summarizing key findings and contributions, emphasizing the success of the proposed PV-UPQC system configuration and control strategy in effectively mitigating power quality issues.

2 Configuration of PV-UPQC system

The Photovoltaic-Unified Power Quality Conditioner (PV-UPQC) is a three-phase system designed to integrate a photovoltaic (PV) array through a shared DC link. This configuration comprises two inverters: a Shunt Active Power Filter (ShAPF) connected in parallel with the AC grid on the load side and a Series Active Power Filter (SeAPF) connected in series with the grid. The solar PV array is directly integrated into the UPQC's DC link via a reverse blocking diode, which prevents the reverse flow of current from the DC link to the PV array. This protection is particularly crucial during low-light or night-time conditions when the PV array might behave as a load instead of a source (refer to Table 1). Inductors are used to interface the compensators with the grid, while a series injection transformer introduces the compensating voltage generated by the SeAPF into the grid. To mitigate harmonics caused by converter switching, LC ripple filters are employed to ensure smoother operation and improved power quality (details in Table 1). [8, 30].

The UPQC serves as a specialized custom power device within electrical power distribution systems, enhancing power quality for consumers. Its applications include the cancellation of current harmonics, compensation of reactive power, elimination of voltage harmonics, improvement of voltage regulation, correction of voltage and current imbalances, rectification of voltage sag or swell, and prevention of voltage interruptions (refer to Figure 1) [1, 8].

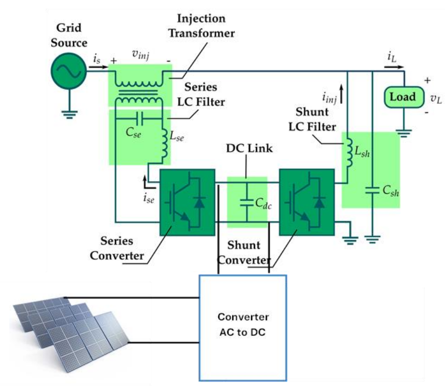

Figure 1: Configuration of PV-UPQC system.

2.1 Design of PV-UPQC

The design process of the PV-UPQC initiates with the proper sizing of key components, including the PV array, DC-link capacitor, and DC-link voltage level. Both the series and shunt compensators are dimensioned to handle the peak power output from the PV array, along with compensating for the reactive power of the load current and mitigating current harmonics. The load configuration entails a nonlinear load featuring a bridge rectifier and a voltage-fed load (Table 1) [1, 8, 30].

PV Array: The chosen PV module is the *1 Soltech 1STH-225-P*. The solar PV array is configured with five strings, each containing 30 SPV modules per string. Comprehensive specifications for both the SPV module and the SPV array can be referenced in Table 2.

3 PV-UPQC system modeling

PV-UPQC is comprised of two crucial subsystems: the shunt compensator and the series compensator. The shunt compensator serves a dual purpose, addressing power quality issues related to load, including load current harmonics and reactive power, while also facilitating power supply from the solar PV array when integrated into PV-UPQC. To harness power from the PV array, the shunt compensator utilizes a maximum power point tracking (MPPT) algorithm.

Table 1: Specifications of Voltage-Fed Load, Bridge Rectifier, Reverse blocking diode, and Ripple filter.

Component	Parameter	Value
Voltage-Fed Load	Power Rating	10 kW
	Operating Voltage	400 V (line-to-line), 230 V (line-to-neutral)
	Power Factor	0.85 (lagging)
	Current	Approx. 14.5 A
Bridge Rectifier	Input Voltage	400 V AC (line-to-line)
	Output Voltage	Approx. 540 V DC
	Output Current	Approx. 18.5 A
	Diode Voltage Drop	1.2 V per diode
	Current Rating	25 A
Reverse blocking diode	Type of Diode	Fast recovery diode
	Voltage Rating	1200 V
	Current Rating	50 A
	Forward Voltage Drop	1-1.2 V
	Thermal Resistance	Low, with a heat sink to manage 25 W dissipation
Ripple filters	Type of filter	LC
	Inductor (L)	27.6 mH
	Capacitor (C)	11.5 mF
	Switching Frequency (f_s)	10 kHz
	Desired current ripple	1.45 A

Table 2: Specifications of Solar PV Array and Module.

Parameter	Value PV Array	Value PV Module
Maximum Power (Pmax)	112.184 kW	224.368 W
Voltage of Open Circuit (Voc)	1.845 kV	36.9 V
Current of Short Circuit (Isc)	80 A	8.09 A
Voltage at Maximum Power Point (Vmpp)	1.48 kV	29.6 V
Current at Maximum Power Point (Impp)	75.9 A	7.59 A
Parallel strings	50	
Series Modules per string	10	

Conversely, the series compensator protects the load against power quality issues originating from the grid, such as sags/swells, by injecting the appropriate voltage in phase with the grid voltage. The focal point of this study is the control of the ShAPF, as illustrated in Figure 2 [3, 4, 7, 15, 20].

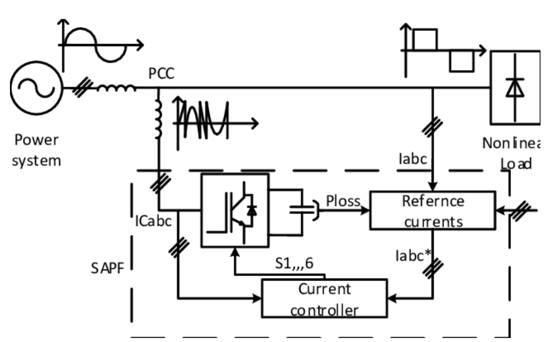

Figure 2: Configuration of the ShAPF.

The configuration of the ShAPF is illustrated in Figure 2. At the heart of the power circuit is a conventional two-level inverter with six IGBTs, controlled using Pulse Width Modulation (PWM) as the modulation technique. In this method, a high-frequency triangular carrier signal is compared with a sinusoidal reference signal to determine the switching states of the IGBTs. The sinusoidal reference signal defines the desired output waveform, while the carrier frequency, typically ranging between 5 kHz and 20 kHz, governs the switching dynamics to balance harmonic mitigation and efficiency. The inverter is connected to the AC grid through a first-order L-type passive filter, characterized by L_f and R_f, which helps attenuate high-frequency switching harmonics. On the DC side, the converter includes a DC-bus capacitor (C_{dc}) to stabilize the DC-link voltage (v_{dc}). According to Kirchhoff's current law, the active filter current is expressed as $i_{fabc} = i_{sabc} - i_{labc}$. To ensure sinusoidal source currents in the *abc*-coordinate system, the ShAPF compensates for harmonic distortions by injecting currents equal in magnitude but opposite in phase to the harmonics generated by the nonlinear load. Beyond harmonic mitigation, the ShAPF also improves the power factor on the grid side by compensating for the reactive power, thereby enhancing overall power quality and grid performance [23, 28, 29, 31].

The power grid comprises three voltages, forming a balanced three-phase system, expressed as follows [2, 7, 8]:

$$\begin{bmatrix} v_{sa} \\ v_{sb} \\ v_{sc} \end{bmatrix} = v_{sm} \begin{bmatrix} \sin(\omega_n t) \\ \sin(\omega_n t - \frac{2\pi}{3}) \\ \sin(\omega_n t + \frac{4\pi}{3}) \end{bmatrix}. \tag{1}$$

The desired source current after compensation can be formulated as per [2, 7, 8]:

$$\begin{bmatrix} i_{sa} \\ i_{sb} \\ i_{sc} \end{bmatrix} = i_{sm} \begin{bmatrix} \sin(\omega_n t) \\ \sin(\omega_n t - \frac{2\pi}{3}) \\ \sin(\omega_n t + \frac{4\pi}{3}) \end{bmatrix}. \tag{2}$$

The current in the three-phase load can be described by its Fourier expansion, as presented in [2, 7, 8]:

$$\begin{bmatrix} i_{la} \\ i_{lb} \\ i_{lc} \end{bmatrix} = \sum_{h=1}^{\infty} i_h i_{lm} \begin{bmatrix} \sin(h\omega_n t + \phi_h) \\ \sin(h\omega_n t + \phi_h - \frac{2\pi}{3}) \\ \sin(h\omega_n t + \phi_h - \frac{4\pi}{3}) \end{bmatrix}, \tag{3}$$

where; v_{sm}; i_{sm} and i_{lm} represent the amplitude of the voltage source and current source and load, respectively, while ω_n denotes the frequency of the system.

The system's dynamic model is defined by a set of differential equations in the (abc) axes, as expressed in equation 4:

$$L_f \frac{d}{dt} \begin{bmatrix} i_{fa} \\ i_{fb} \\ i_{fc} \\ v_{dc} \end{bmatrix} = -R_f \begin{bmatrix} i_{fa} \\ i_{fb} \\ i_{fc} \\ \frac{L_f}{C_{dc} R_f} i_{dc} \end{bmatrix} + \begin{bmatrix} v_{fa} \\ v_{fb} \\ v_{fc} \\ 0 \end{bmatrix} - \begin{bmatrix} v_{la} \\ v_{lb} \\ v_{lc} \\ 0 \end{bmatrix}. \tag{4}$$

The relationship between the ShAPF and the grid is characterized through the average dynamic model expressed in $d-q$ coordinates, as outlined below [1, 20, 30]:

$$\begin{bmatrix} \dot{i}_{fd} \\ \dot{i}_{fq} \\ \dot{v}_{dc} \end{bmatrix} = \begin{bmatrix} \frac{-R_f}{L_f} & \omega_s & 0 \\ -\omega_s & \frac{-R_f}{L_f} & 0 \\ 0 & 0 & \frac{1}{C_{dc}} \end{bmatrix} \begin{bmatrix} i_{fd} \\ i_{fq} \\ i_{dc} \end{bmatrix} + \begin{bmatrix} \frac{1}{L_f} & 0 & 0 \\ 0 & \frac{1}{L_f} & 0 \\ 0 & 0 & 0 \end{bmatrix} \begin{bmatrix} v_{fd} \\ v_{fq} \\ 0 \end{bmatrix} - \begin{bmatrix} \frac{1}{L_f} & 0 & 0 \\ 0 & \frac{1}{L_f} & 0 \\ 0 & 0 & 0 \end{bmatrix} \begin{bmatrix} v_{ld} \\ v_{lq} \\ 0 \end{bmatrix}. \tag{5}$$

The time derivatives of the i_{ld} and i_{lq} currents can be expressed as the sum of two components: a continuous component and an alternate component [5, 7, 14]:

$$\begin{bmatrix} i_{ld} \\ i_{lq} \end{bmatrix} = \begin{bmatrix} \bar{i}_{ld} + \tilde{i}_{ld} \\ \bar{i}_{lf} + \tilde{i}_{lf} \end{bmatrix}. \tag{6}$$

The system defined in equation 4 represents a multi-input multi-output nonlinear system. To apply SM-C to the three-phase ShAPF, it is necessary to decompose this system into two subsystems [2, 7, 8]:

<u>Subsystem (A)</u>: In the first subsystem specified by equation 5, the control variables are designated as the voltages v_{fd}, v_{fq}, and the filter's outputs are identified as the currents i_{fd}, i_{fq} [20]:

$$\begin{bmatrix} \dot{i}_{fd} \\ \dot{i}_{fq} \end{bmatrix} = \begin{bmatrix} \frac{-R_f}{L_f} & \omega_s \\ -\omega_s & \frac{-R_f}{L_f} \end{bmatrix} \begin{bmatrix} i_{fd} \\ i_{fq} \end{bmatrix} + \begin{bmatrix} \frac{1}{L_f} & 0 \\ 0 & \frac{1}{L_f} \end{bmatrix} \begin{bmatrix} v_{fd} \\ v_{fq} \end{bmatrix} - \begin{bmatrix} \frac{1}{L_f} & 0 \\ 0 & \frac{1}{L_f} \end{bmatrix} \begin{bmatrix} v_{ld} \\ v_{lq} \end{bmatrix}. \tag{7}$$

Subsystem (B): The secondary subsystem's mathematical representation can be articulated as follows [6]:

$$\begin{bmatrix} \dot{v}_{dc} \\ 0 \end{bmatrix} = \frac{1}{C_{dc}} \begin{bmatrix} i_{dc} \\ 0 \end{bmatrix}. \tag{8}$$

In this subsystem, the current in i_{dc} is considered as the control variable, and the voltage v_{dc} is identified as the output variable.

The model maintains its consistency over time within a particular switching state. To provide a clear representation, the model is formulated in the general format as outlined in [2, 7, 8].

$$\dot{X} = AX + BU + D \tag{9}$$

where; $X = \begin{bmatrix} x_1 \\ x_2 \end{bmatrix} = \begin{bmatrix} i_{fd} \\ i_{fq} \end{bmatrix}$; $A = \begin{bmatrix} -\frac{R_r}{L_f} & \omega_s \\ -\omega_s & -\frac{R_r}{L_f} \end{bmatrix}$; $B = \begin{bmatrix} \frac{1}{L_f} & 0 \\ 0 & \frac{1}{L_f} \end{bmatrix}$; $D = \begin{bmatrix} \frac{1}{L_f} & 0 \\ 0 & \frac{1}{L_f} \end{bmatrix}$.

4 Control strategy of PV-UPQC

4.1 Harmonics identification (harmonic extraction)

Precise estimation and extraction of harmonics are critical for evaluating the performance of the ShAPF. To determine the reference current, various methodologies are applied, generally categorized into time-domain and frequency-domain analyses. Time-domain analysis, which utilizes algebraic transformations and circuit principles, offers a direct and computationally efficient approach, resulting in faster control processing. In contrast, frequency-domain analysis involves a more complex process, demanding greater computational resources and memory capacity [24, 27]. This research adopts the instantaneous active and reactive power theory, commonly known as $P-Q$ theory, within the time domain. A corresponding simulation model has been developed using MATLAB/Simulink. The core principle of $P-Q$ theory involves converting the stationary $a-b-c$ reference frame into the $\alpha-\beta$ rotating reference frame using the Clarke transformation (equation 10) [27]. This transformation effectively removes the DC component from the instantaneous calculations of active (P) and reactive (Q) power. The detailed configuration of this methodology is illustrated in Figure 3, which demonstrates the $P-Q$ Harmonic Current Extraction Theory [24].

$$\begin{bmatrix} \alpha \\ \beta \end{bmatrix} = \frac{2}{3} \begin{bmatrix} 1 & -\frac{1}{2} & -\frac{1}{2} \\ 0 & \frac{\sqrt{3}}{2} & -\frac{\sqrt{3}}{2} \\ \frac{1}{\sqrt{2}} & \frac{1}{\sqrt{2}} & \frac{1}{\sqrt{2}} \end{bmatrix} \begin{bmatrix} a \\ b \\ c \end{bmatrix}. \tag{10}$$

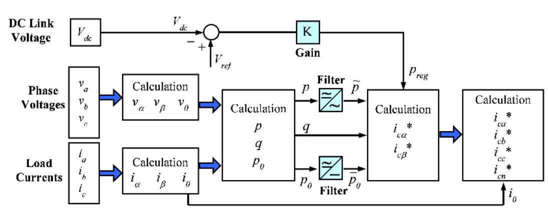

Figure 3: Harmonics extraction by $P-Q$ theory.

4.2 Sliding mode control for ShAPF

The Sliding Mode Control (SM-C) strategy stands out as a widely adopted nonlinear control technique due to its resilience to variable parameters in regulating complex systems. A distinctive feature of SM-C is its capability to compel the trajectory dynamics of the controlled system to adhere to a specific sliding surface until reaching equilibrium [17, 26]. However, a notable drawback of the sliding modes method is its adverse impact on the power grid's quality, resulting from mechanical issues and undesirable fluctuations, commonly referred to as chattering. In recent years, there has been an increased focus on mitigating these challenges, making sliding mode an increasingly attractive solution [25, 26]. Furthermore, the design of SM-C primarily involves three key stages: the selection of the sliding surface, the identification of existing conditions, and the synthesis of control laws. The existence of sliding mode is contingent upon specific conditions (The Lyapunov function) [12, 25]:

$$S\dot{S} < 0. \tag{11}$$

The formulation of the nonlinear expression for the sliding surface (Slotine) was derived [26]:

$$s(t) = (\lambda_s + \frac{d}{dt})^{n-1} e(t), \tag{12}$$

where; $\lambda_s > 0$, $r(t)$ and $y(t)$ were, desired and real dynamic, respectively; n: the relative degree, $e(t)$: error of the variable to be adjusted; $e(t) = y(t) - r(t)$.

The primary objective of the three-phase ShAPF is to tackle the harmonics and reactive power demands originating from the nonlinear load. The synthesis of the controller involves the cascading of two loops. Initially, an inner current loop is formed by two non-linear regulators, aimed at compensating for reactive and harmonic power. This facilitates achieving sinusoidal input currents synchronized with the grid voltages. Subsequently, an external loop is established to ensure voltage control on the DC side of the ShAPF, contributing to enhancing the overall performance of the system [2, 7, 20]:

4.2.1 Creating the internal loop for current control

The initial phase of the design process entails choosing switching surfaces for the current inner loop. The sliding mode functions, crafted for tracking the reference electric current, are identified. The global sliding surface is formed by combining the classical sliding surface (Slotine's method in equation 12) with an integral term. In our case, where the relative degree $n = 1$, it is expressed as [2, 7, 20]:

$$S(X) = k_p E(X) + k_i \int e(X) dt. \tag{13}$$

The switching surface, when $n = 1$ is substituted into (equation 12), is obtained as:

$$s(t) = e(X) = (X^* - X). \tag{14}$$

The errors in tracking the currents i_{fd} , i_{fq} [5, 6]:

$$\begin{bmatrix} e(i_{fd}) \\ e(i_{fq}) \end{bmatrix} = \begin{bmatrix} (i^*_{fd} - i_{fd}) \\ (i^*_{fq} - i_{fq}) \end{bmatrix}. \tag{15}$$

If we replace equation 1 with equation 7, we obtain:

$$\begin{bmatrix} i^*_{fd} - i_{fd} \\ i^*_{fq} - i_{fq} \end{bmatrix} = \begin{bmatrix} i^*_{fd} \\ i^*_{fq} \end{bmatrix} - \left(\begin{bmatrix} \frac{-R_f}{L_f} & \omega_s \\ -\omega_s & \frac{-R_f}{L_f} \end{bmatrix} \begin{bmatrix} i_{fd} \\ i_{fq} \end{bmatrix} + \begin{bmatrix} \frac{1}{L_f} & 0 \\ 0 & \frac{1}{L_f} \end{bmatrix} \begin{bmatrix} v^*_{fd} \\ v^*_{fq} \end{bmatrix} - \begin{bmatrix} \frac{1}{L_f} & 0 \\ 0 & \frac{1}{L_f} \end{bmatrix} \begin{bmatrix} v_{ld} \\ v_{lq} \end{bmatrix} \right). \tag{16}$$

The development of the sliding surfaces can be deduced from equations 13 and 14 in the subsequent manner:

$$\begin{bmatrix} S(i_{fd}) \\ S(i_{fq}) \end{bmatrix} = \begin{bmatrix} k_d & k_{id} \\ k_q & k_{iq} \end{bmatrix} \begin{bmatrix} (i^*_{fd} - i_{fd}) & (i^*_{fq} - i_{fq}) \\ \int (i^*_{fd} - i_{fd}) dt & \int (i^*_{fq} - i_{fq}) dt \end{bmatrix}. \tag{17}$$

In the ISM-C, the conditions are such that: $\begin{bmatrix} S(i_{fd}) \\ S(i_{fq}) \end{bmatrix} = \begin{bmatrix} 0 \\ 0 \end{bmatrix}$ and $\begin{bmatrix} \dot{S}(i_{fd}) \\ \dot{S}(i_{fq}) \end{bmatrix} = \begin{bmatrix} 0 \\ 0 \end{bmatrix}$. Following that, the formulations for the two sliding surfaces are articulated as follows [2, 7]:

$$\begin{bmatrix} S(i_{fd}) \\ S(i_{fq}) \end{bmatrix} = \begin{bmatrix} k_d & k_{id} \\ k_q & k_{iq} \end{bmatrix} \begin{bmatrix} (i^*_{fd} - i_{fd}) & (i^*_{fq} - i_{fq}) \\ \int (i^*_{fd} - i_{fd}) dt & \int (i^*_{fq} - i_{fq}) dt \end{bmatrix} = \begin{bmatrix} 0 \\ 0 \end{bmatrix}. \tag{18}$$

The derivative of $S(i_{fd})$ and $S(i_{fq})$ with respect to time is expressed by:

$$\begin{bmatrix} \dot{S}(i_{fd}) \\ \dot{S}(i_{fq}) \end{bmatrix} = \begin{bmatrix} k_d & k_{id} \\ k_q & k_{iq} \end{bmatrix} \begin{bmatrix} (\dot{i}^*_{fd} - \dot{i}_{fd}) & (\dot{i}^*_{fq} - \dot{i}_{fq}) \\ (i^*_{fd} - i_{fd}) & (i^*_{fq} - i_{fq}) \end{bmatrix} = \begin{bmatrix} 0 \\ 0 \end{bmatrix}. \tag{19}$$

Upon reformulating equation 19, we acquire [6, 20]:

$$\begin{bmatrix} \dot{S}(i_{fd}) \\ \dot{S}(i_{fq}) \end{bmatrix} = \begin{bmatrix} k_d & 0 \\ 0 & k_q \end{bmatrix} \begin{bmatrix} (\dot{i}^*_{fd} - \dot{i}_{fd}) \\ (i^*_{fq} - i_{fq}) \end{bmatrix} + \begin{bmatrix} k_{id} & 0 \\ 0 & k_{iq} \end{bmatrix} \begin{bmatrix} (\dot{i}^*_{fd} - \dot{i}_{fd}) \\ (i^*_{fq} - i_{fq}) \end{bmatrix} = \begin{bmatrix} 0 \\ 0 \end{bmatrix}. \tag{20}$$

We substitute equation 16 into equation 20:

$$\begin{bmatrix} \dot{S}(i_{fd}) \\ \dot{S}(i_{fq}) \end{bmatrix} = \begin{bmatrix} k_d & 0 \\ 0 & k_q \end{bmatrix} \left(\begin{bmatrix} i^*_{fd} \\ i^*_{fq} \end{bmatrix} - \left(\begin{bmatrix} \frac{-R_f}{L_f} & \omega_s \\ -\omega_s & \frac{-R_f}{L_f} \end{bmatrix} \begin{bmatrix} i_{fd} \\ i_{fq} \end{bmatrix} + \begin{bmatrix} \frac{1}{L_f} & 0 \\ 0 & \frac{1}{L_f} \end{bmatrix} \begin{bmatrix} v^*_{fd} \\ v^*_{fq} \end{bmatrix} - \begin{bmatrix} \frac{1}{L_f} & 0 \\ 0 & \frac{1}{L_f} \end{bmatrix} \begin{bmatrix} v_{ld} \\ v_{lq} \end{bmatrix} \right) \right),$$

$$+ \begin{bmatrix} k_{id} & 0 \\ 0 & k_{iq} \end{bmatrix} \begin{bmatrix} (\dot{i}^*_{fd} - \dot{i}_{fd}) \\ (i^*_{fq} - i_{fq}) \end{bmatrix} = \begin{bmatrix} 0 \\ 0 \end{bmatrix}. \tag{21}$$

The control law "u" can be decomposed into two components: the first: discontinuous control u_{dis}, the second is equivalent control u_{eq}:

$$u = u_{eq} + u_{dis} = \begin{bmatrix} u^{eq}_{fd} + u^{dis}_{fd} \\ u^{eq}_{fq} + u^{dis}_{fq} \end{bmatrix} = \begin{bmatrix} v^*_{fd} \\ v^*_{fq} \end{bmatrix}. \tag{22}$$

a) Equivalent law

As derived from equation 21, the equivalent control terms u^{eq}_{fd} and u^{eq}_{fq} are expressed as follows [6]:

$$\begin{bmatrix} u^{eq}_{fd} \\ u^{eq}_{fq} \end{bmatrix} = \begin{bmatrix} v^{eq}_{fd} \\ v^{eq}_{fq} \end{bmatrix} \left(\begin{bmatrix} k_d & 0 \\ 0 & k_q \end{bmatrix} \begin{bmatrix} \frac{1}{L_f} & 0 \\ 0 & \frac{1}{L_f} \end{bmatrix} \right) - \begin{bmatrix} k_{id} & 0 \\ 0 & k_{iq} \end{bmatrix} \begin{bmatrix} (\dot{i}^*_{fd} - \dot{i}_{fd}) \\ (i^*_{fq} - i_{fq}) \end{bmatrix} = \begin{bmatrix} k_d & 0 \\ 0 & k_q \end{bmatrix} \begin{bmatrix} i^*_{fd} \\ i^*_{fq} \end{bmatrix} -$$

$$\begin{bmatrix} k_d & 0 \\ 0 & k_q \end{bmatrix} \left(\begin{bmatrix} \frac{-R_f}{L_f} & \omega_s \\ -\omega_s & \frac{-R_f}{L_f} \end{bmatrix} \begin{bmatrix} i_{fd} \\ i_{fq} \end{bmatrix} - \begin{bmatrix} \frac{1}{L_f} & 0 \\ 0 & \frac{1}{L_f} \end{bmatrix} \begin{bmatrix} v_{ld} \\ v_{lq} \end{bmatrix} \right). \tag{23}$$

b) Discontinuous law

When the state trajectory diverges from the sliding surface, a discontinuous control is applied to minimize the deviation and guide the trajectory back to the sliding surface. This ensures convergence to the reference trajectory. The formulation of this control function is detailed in [5, 6, 20].

$$\begin{cases} u^{dis}_{fd} = \begin{bmatrix} U_{max} & 0 \\ 0 & -U_{max} \end{bmatrix} \begin{bmatrix} satS(i_{fd}) \\ satS(i_{fd}) \end{bmatrix} & \begin{matrix} \text{if } S(i_{fd}) > 0 \\ \text{if } S(i_{fd}) < 0 \end{matrix} \\ \\ u^{dis}_{fq} = \begin{bmatrix} U_{max} & 0 \\ 0 & -U_{max} \end{bmatrix} \begin{bmatrix} satS(i_{fq}) \\ satS(i_{fq}) \end{bmatrix} & \begin{matrix} \text{if } S(i_{fq}) > 0 \\ \text{if } S(i_{fq}) < 0 \end{matrix} \end{cases} \tag{24}$$

where the discontinuous control function is $u(t) = -Ksat(S(x(t)))$ for $S(x(t)) \neq 0$, whit $u(t)$ is the control input, K is a positive constant gain, and $sat(x)$ is the saturation function.

The control can be articulated as follows:

$$\begin{bmatrix} v^*_{fd} \\ v^*_{fq} \end{bmatrix} = \begin{bmatrix} u_{fd} \\ u_{fq} \end{bmatrix} = \begin{bmatrix} u^{eq}_{fd} \\ u^{eq}_{fq} \end{bmatrix} + \begin{bmatrix} u^{dis}_{fd} \\ u^{dis}_{fq} \end{bmatrix}. \tag{25}$$

Figure 4 illustrates the inner current control loop utilizing an ISM-C:

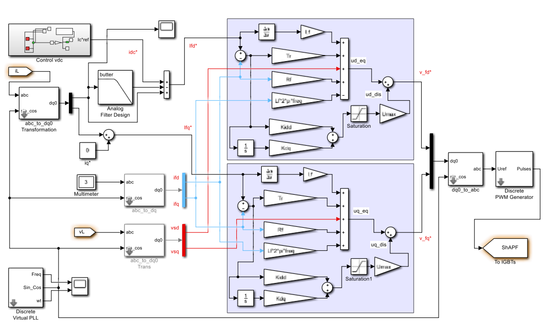

Figure 4: The internal loop for current control using ISM-C.

The Grey Wolf Optimizer (GWO) algorithm is employed in the next section to optimize the gains parameters of ISM-C in the inner current control, including k_d, k_q, k_{id}, k_{iq}, and U_{max}. This optimization process is discussed in detail in the following sections.

4.2.2 Creating the external loop for DC Voltage control

The ShAPF employs sliding mode control (SM-C) to regulate the DC-link voltage, ensuring stability and effective harmonic current compensation. By comparing the actual voltage with a reference value ($e(v_{dc}) = v^*_{dc} - v_{dc}$), the SM-C minimizes steady-state errors and maintains robust voltage regulation. This design compensates for inverter switching losses and supports efficient system operation [2]. The sliding surface equation governing the DC voltage control is detailed in [6].

$$\left[\ S(v_{dc})\ \right] = \left[\ k_{dc1} \quad k_{dc2} \quad k_{dc3}\ \right] \begin{bmatrix} e(v_{dc}) \\ \dot{e}(v_{dc}) \\ \int e(v_{dc}) \end{bmatrix}. \tag{26}$$

In ISM-C, the definitions of the switching functions u_1 and u_2 are as follows for the regulation of the capacitor's DC voltage (v_{dc}) [2, 6, 7]:

$$\begin{cases} u_1 = \begin{bmatrix} U_{1-max} \\ -U_{1-max} \end{bmatrix} & \begin{matrix} \text{if } S(e(v_{dc}))e(v_{dc}) > 0 \\ \text{if } S(e(v_{dc}))e(v_{dc}) < 0 \end{matrix} \\ u_2 = \begin{bmatrix} U_{2-max} \\ -U_{2-max} \end{bmatrix} & \begin{matrix} \text{if } S(e(v_{dc}))\dot{e}(v_{dc}) > 0 \\ \text{if } S(e(v_{dc}))\dot{e}(v_{dc}) < 0 \end{matrix} \end{cases} \tag{27}$$

Hence, the output of this ISM-C is specified as:

$$\left[\ u_{v_{dc}}\ \right] = \left[\ i_{dc}\ \right] = \left[\ k_{dc4} \quad k_{dc5}\ \right] \begin{bmatrix} e(v_{dc})u_1 \\ \dot{e}(v_{dc})u_2 \end{bmatrix}. \tag{28}$$

The Grey Wolf Optimizer (GWO) algorithm is employed in the next section to optimize the gains parameters of ISM-C in the inner current control, including k_{dc1}, k_{dc2}, k_{dc3}, k_{dc4}, k_{dc5}, u_{1-max}, and u_{2-max}. This optimization process is discussed in detail in the following sections.

Figure 5 depicts the external voltage control loop for the DC voltage employing ISM-C.

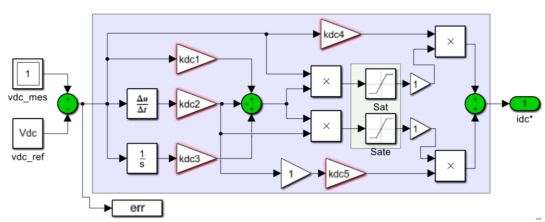

Figure 5: The external loop for DC voltage control using ISM-C.

The hybrid neuro-fuzzy (HNF) approach integrates fuzzy and neural techniques to enhance sliding mode control (SM-C) by minimizing chattering effects during harmonic mitigation with the ShAPF. This method addresses power quality issues caused by nonlinear loads, which impact the stability of the distribution network. By replacing the discontinuous term (Sat function) in the control law, the HNF approach effectively reduces chattering, even under variations in irradiation and temperature, while maintaining robust harmonic suppression.

4.3 Hybrid neuro-fuzzy-integral sliding mode control (HNF-ISM-C)

In recent times, there has been a growing trend in employing artificial intelligence strategies that combine fuzzy logic (FL) and neural networks [6, 15, 24, 27]. Fuzzy logic controllers have demonstrated exceptional and rapid control capabilities [6]. One notable advantage is their ability to operate without the need for a precise mathematical model of the system, showcasing high performance in multidimensional, complex, and nonlinear systems [15, 18]. Additionally, fuzzy rules offer a more coherent description of real processes. However, a drawback of fuzzy logic lies in the meticulous and coordinated definition of a set of rules, along with the assembly of membership functions, within a limited timeframe compared to the preceding processes. Furthermore, the use of artificial neural networks (ANN) alone may fall short in adjusting all operational states in cases of insufficient training data [9, 16].

In a prior study, a hybrid system named HNF was proposed, combining fuzzy systems with neural networks to leverage the advantages of both techniques – the learning ability of ANN and the reasoning ability of rule-based FLC [25].

The fuzzy logic controller comprises five key components: the fuzzification of input variables, the application of fuzzy operators (Or/And) in the preceding stage, the modulation from the antecedents to the consequents, the compilation of rule consequences outlined in Table 3 based on linguistic information derived from the dynamic behavior system, and ultimately, the defuzzification process involving two inputs and one output. The block diagram of the fuzzy logic controller (FLC) is illustrated in Figure 6 [6, 15].

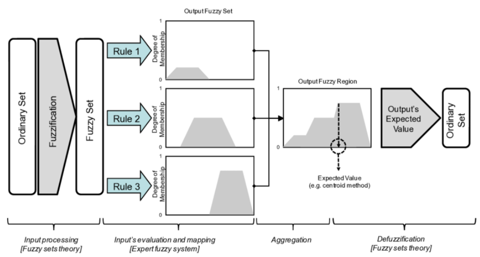

Figure 6: The block diagram of the FLC.

The fuzzy system, constructed using the rule base in Table 3, employs a Mamdani-type fuzzy logic system. The output membership function is generated using the maximum technique, and defuzzification is performed with the centroid operator. Table 3 provides the detailed FLC parameters [25]:

Table 3: Rule basis and parameters of FLC.

DE/E	N	Z	P
N	BN	MN	Z
Z	MN	Z	MP
P	Z	MP	BP
FLC Parameters			
FIS type		Mamdani	
And method		Min	
Or method		Max	
Implication		Min	
Aggregation		Max	
Defuzzification		Centroid	

With, BN: Big Negative, Z: Zero, MN: Medium Negative, MN: Medium Negative, MP: Medium Positive.

4.3.1 Design of HNF controller

The HNF framework is organized into five layers, mirroring the structural design of the Sugeno Fuzzy (SF) model [25]. The first layer serves to represent the inputs, with the second layer performing fuzzification. Layers three and four are responsible for estimating fuzzy rules, while the fifth layer executes defuzzification, delivering the final output. The detailed architecture of the HNF system is illustrated in Figure 7 [25]. The effectiveness of the HNF system is largely determined by the transfer function coefficients and the input membership functions. This configuration incorporates three membership functions (Positive, Zero, Negative), two input parameters (error and the rate of change of error), and a set of nine rules [25].

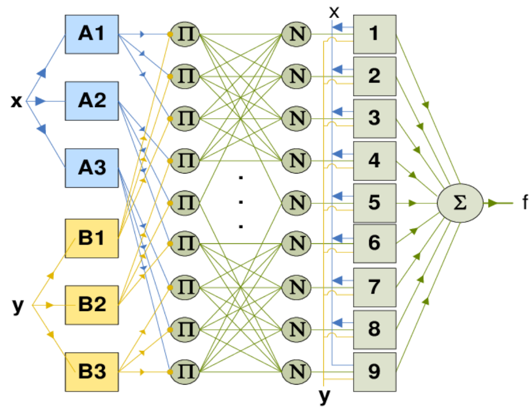

Figure 7: Structure of HNF controller.

The Hybrid Neuro-Fuzzy Integral Sliding Mode Controller (HNF-ISM-C) is an advanced adaptation of the conventional sliding mode controller (SMC). In this approach, the traditional switching control term, typically represented as sat(S(x)), is replaced with an input derived from the HNF controller. This innovative technique, termed HNF-ISM-C, aims to enhance the performance of the PV-UPQC system while effectively addressing the chattering phenomenon inherent to traditional SMC. The HNF-ISM-C is specifically designed to improve power quality, stabilize the distribution network, and minimize harmonics caused by nonlinear loads using the ShAPF. Its robust structure, which integrates the learning capability of neuro-fuzzy systems with the stability of sliding mode control, is depicted in Figure 8. This synergistic design optimizes system response and ensures reliable operation under varying load and environmental conditions.

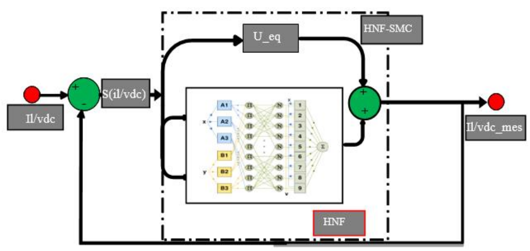

Figure 8: The HNF-ISM-C configuration for ShAPF.

This holistic approach represents a noteworthy advancement in the field, providing a more sophisticated and effective solution for the seamless integration of PV solar into the electrical grid. Simultaneously, it addresses potential issues related to power quality, stability, and harmonics.

a) The control strategy provided by HNF-ISM-C for currents is as follows:

$$\begin{bmatrix} v_{fd}^* \\ v_{fq}^* \end{bmatrix} = \begin{bmatrix} u_{fd} \\ u_{fq} \end{bmatrix} = \begin{bmatrix} u_{fd}^{eq} \\ u_{fq}^{eq} \end{bmatrix} + \begin{bmatrix} u_{fd}^{dis-ANFIS} \\ u_{fq}^{dis-ANFIS} \end{bmatrix}. \tag{29}$$

b) The control strategy provided by HNF-ISM-C for v_{dc} is as follows:

$$\begin{bmatrix} u_{v_{dc}} \end{bmatrix} = \begin{bmatrix} i_{dc} \end{bmatrix} = \begin{bmatrix} k_{dc4} & k_{dc5} \end{bmatrix} \begin{bmatrix} u_{dc1}^{dis-ANFIS}(v_{dc}^* - v_{dc}) \\ u_{dc2}^{dis-ANFIS} d\frac{(v_{dc}^* - v_{dc})}{dt} \end{bmatrix}. \tag{30}$$

The key challenge in implementing ISM-C based on the HNF algorithm lies in identifying optimal parameters. Achieving optimal performance and efficiency of the control system requires determining suitable parameter values. To tackle this challenge, this study suggests employing the Grey Wolf Optimizer (GWO) tuning approach. GWO acts as a tuning mechanism to fine-tune the parameters, ensuring the effectiveness of HNF-ISM-C in mitigating undesired effects and enhancing power quality.

4.4 Algorithm of grey wolf optimizer

The Grey Wolf Optimizer (GWO) algorithm, introduced by Mirjalili and colleagues in 2014, stands as a contemporary and efficient swarm intelligence technique. Inspired by the social hierarchy and hunting patterns of grey wolves [10, 11, 22, 32], this algorithm effectively replicates natural behaviors for optimization purposes. Notably, it has demonstrated accuracy in performance when compared with conventional algorithms such as Genetic Algorithms (GA) [13], Differential Calculus (DC), Particle Swarm Optimization (PSO) [15], and Simulated Annealing (SI).

The distinctive aspect of the GWO algorithm lies in its emulation of socially dominant behavior within an average group size of 5 to 12 wolves. This dominance is structured in a pyramid-like hierarchy with different levels, as depicted in Figure 9 [22, 32]. This organizational feature adds an intriguing dimension to the algorithm's functioning, contributing to its effectiveness in optimization tasks.

Figure 9: The structured order of GWO.

Grey wolves display a hunting behavior that involves tracking, pursuing, surrounding, and ultimately attacking their prey. In their social structure, there are typically four types of wolves organized in a hierarchical manner, as depicted in Table 4 [10, 11]:

Table 4: The functions are performed by the four types of grey wolves.

Alpha Wolves:	* Leaders of the group and hold the highest position in the food chain. * Assume the role of decision-makers within the pack.
Beta Wolves:	* Positioned one level below the Alpha wolves. * Serve as supporting figures in decision-making processes.
Delta Wolves:	* Found in the third tier of the hierarchy. * Tasked with sending out wolf scouts for various missions.
Omega Wolves:	* Occupy the lowest tier in the hierarchy. * Follow the orders and guidance of the dominant wolves.

The visual representation for implementing the GWO algorithm is depicted in Figure 10 [11, 32]:

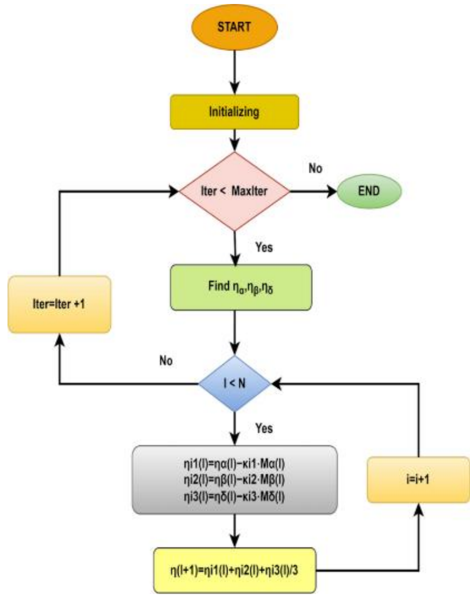

Figure 10: Algorithm of GWO.

In this study, the parameters of the HNF-ISM-C (k_d, k_q, k_{id}, k_{iq}, U_{max}, k_{dc1}, k_{dc2}, k_{dc3}, k_{dc4}, k_{dc5}, u_{1-max}, and u_{2-max}) for PV-UPQC are optimized using the Grey Wolf Optimizer (GWO) algorithm. The GWO algorithm is selected to achieve the optimization objective of minimizing a cost function, which is defined as the sum of squared control errors. Figure 11 illustrates the comprehensive PV-UPQC system incorporating the HNF-ISM-C strategy with GWO-optimized parameter gains. The evaluation of this system is conducted under real irradiation and temperature conditions in the Adrar region of Algeria.

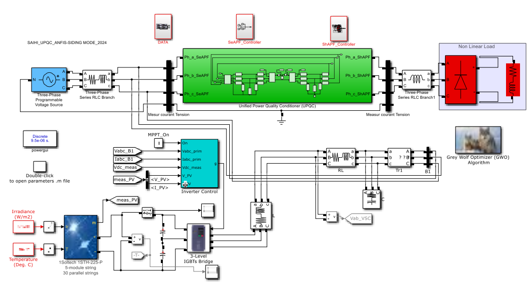

Figure 11: PV-UPQC using HNF-ISM-C/GWO.

5 Data and site location

The Adrar region, situated in the southwestern part of Algeria, is depicted in Figure 12. This area is known for its substantial average solar irradiation and temperature [21, 25]. The study relies on data obtained from the Renewable Energy Research Unit in the Saharan Environment (URER/MS) station, located in Adrar and affiliated with the Algiers Renewable Energy Development Center (CDER). Positioned at 27.52° N, 0.18° W, and an elevation of 292 m, the station utilizes various instruments for assessing solar radiation. CM11 Kipp & Zonen pyranometers are employed to measure global solar radiation on both horizontal and inclined surfaces (Figure 12 a and b). The station features a sun tracker, Eppley NIP Pyrheliometer for direct solar radiation (Figure 12 c and d), a pyranometer with a shadow band for diffuse radiation, and a Type J thermocouple for temperature (Figure 12 e). Additionally, a photovoltaic solar kit ensures energy self-sufficiency. Figure 12 provides an overview of the meteorological station [21, 25].

Figure 13 depicts the recorded irradiation and temperature data in Adrar on Mai 23, 2023, covering the time from 6 am to 8 pm.

(a) Geographical Adrar location.

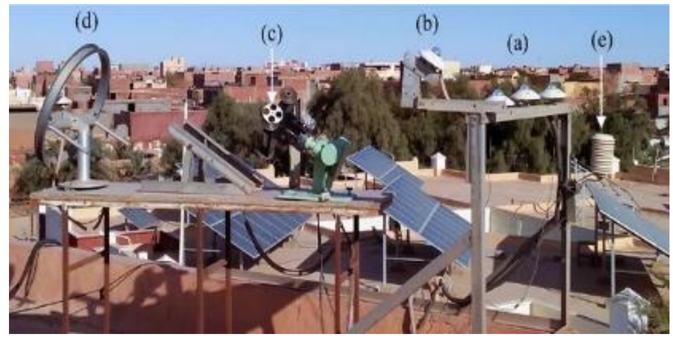

(b) Station of URER-MS.

Figure 12: Station of URER-MS.

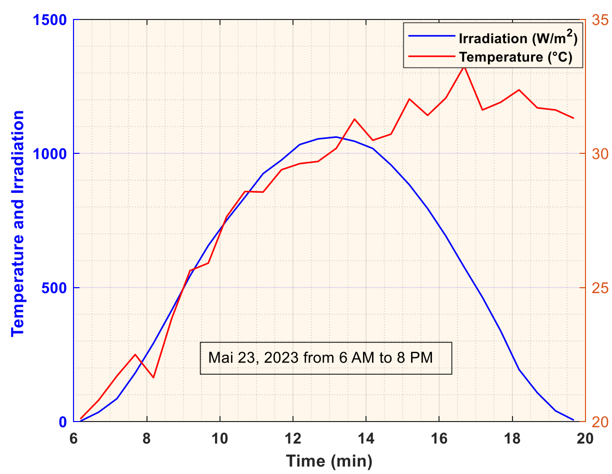

Figure 13: Irradiation and temperature measurements obtained from the URERMS station.

6 Simulations result

In this section, we delve into the numerical simulations conducted to assess the PV-UPQC system's performance using the Power Systems Toolbox. Figure 11 provides a visual representation of the system's behavior both pre- and post-integration of the ShAPF, facilitating a comparative analysis among the PI controller, classical SMC, and the novel HNF-ISM-C. Crucial system parameters are outlined in Table 5, offering valuable insights into the simulation configuration. Furthermore, to optimize the controller gains and elevate system efficiency, we employ the Grey Wolf Optimizer (GWO), as shown in Table 6. Through meticulous examination and comparison, we aim to evaluate the effectiveness of various control strategies in achieving desired system outcomes, Table 7. Presents the PI parameter values tuned using the GWO method.

Figure 14 illustrates the source voltages, showcasing sinusoidal waveforms with a magnitude of $\frac{380}{\sqrt{2}}$ V.

6.1 Pre-filtering

In Figure 15 (a), the waveforms of both the source and load currents are depicted, showcasing highly non-sinusoidal and distorted currents that do not align with the corresponding voltages. Furthermore, Figure 15 (b) highlights a significant discrepancy between reactive and active power, with reactive power dominating, thus adversely affecting grid power quality. Additionally, Figure 15 (c) demonstrates poor power factor quality without the ShAPF, ranging from 57% to 67%. Figure 15 (d) further emphasizes the issue by presenting the total harmonic distortion (THD) of the first-phase

Table 5: System parameters values.

Parameters	Symbol	Values
Network	E	$\frac{380}{\sqrt{2}}$ V
	F	50 Hz
Load Resistor	Rf	0.0080 Ω
Load Inductance	Lf	0.0059 H
Load Capacitor	Cf	0 μ H
Filter Resistor	RL	0.0080 Ω
Filter Inductance	LL	0.0029 H
Filter Capacitor	CL	5.9422 μ H
DC-link Voltage	vdc	850 V

Table 6: GWO Parameter values.

Parameters	GWO
No of iterations	100
Size of population	4
Dimension	12
Lower bound	[0 0 0 0 0 0 0 0 0 0 0 0]
Upper bound	[450 350 490 340 400 300 450 2 2 25 4]
GWO current	$[k_d, k_q, k_{id}, k_{iq}, k_{dc1}, k_{dc2}, k_{dc3}, k_{dc4}, k_{dc5}, U_{max}, u_{1-max}, u_{2-max}]$

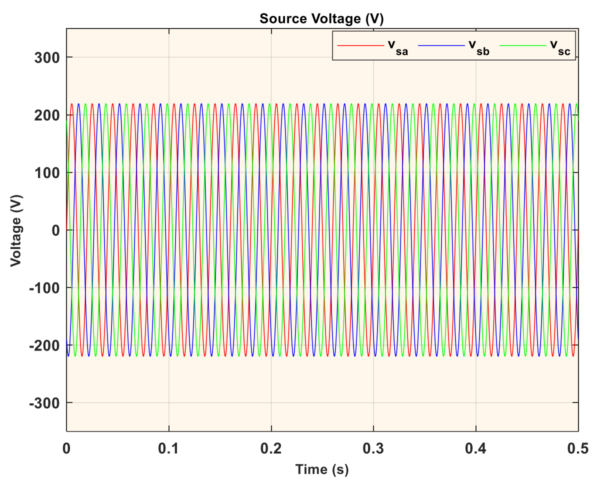

Figure 14: Source voltage.

source current, measured at 31.92%, indicating substantial degradation in power quality when the ShAPF is absent. The subsequent section delves into the integration of the ShAPF to improve power quality and attenuate harmonic currents.

Table 7: PI parameter values tuned using the GWO method.

Parameters	Integral gain (k_i)	Proportional gain (k_p)
Filter PI gains	$1.9298e^{+03}$	1.5215
DC link PI gains	311.9802	2.3171

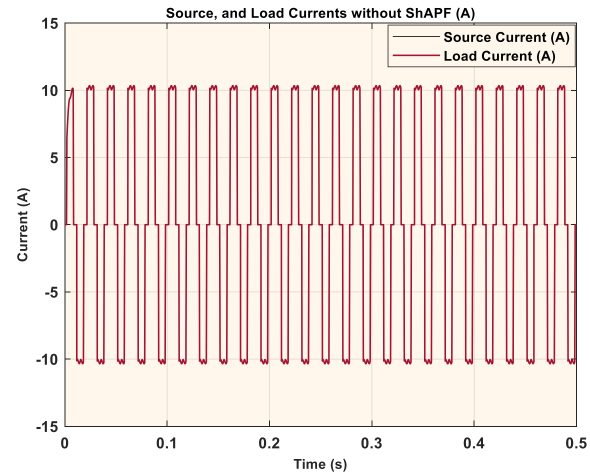

(a) **Source, and load currents.**

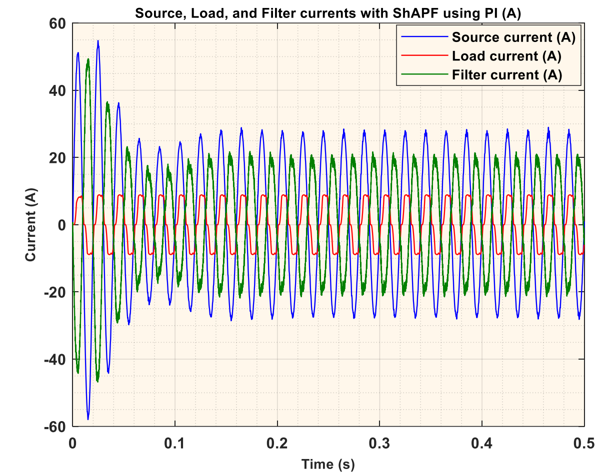

(a) **Source, and load currents.**

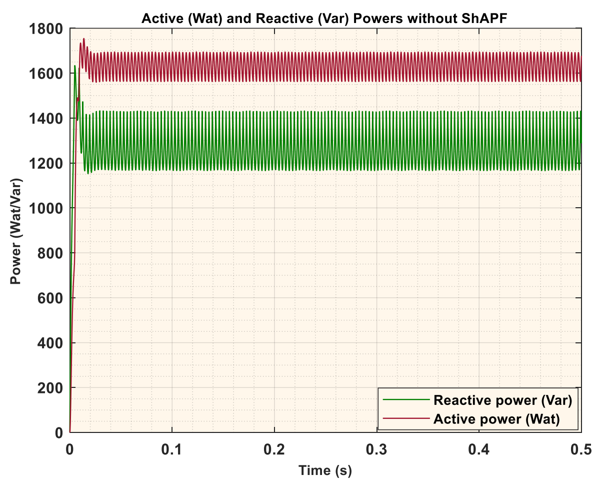

(b) **Active, and reactive powers.**

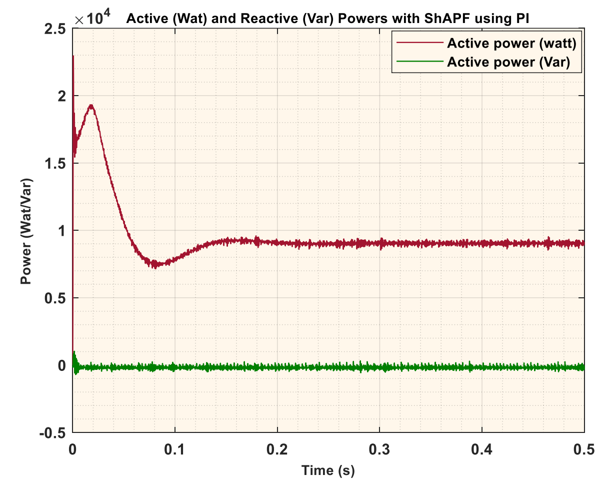

(b) **Active, and reactive powers.**

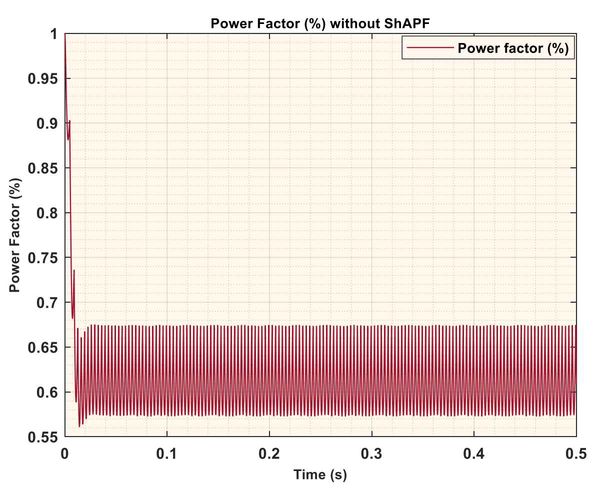

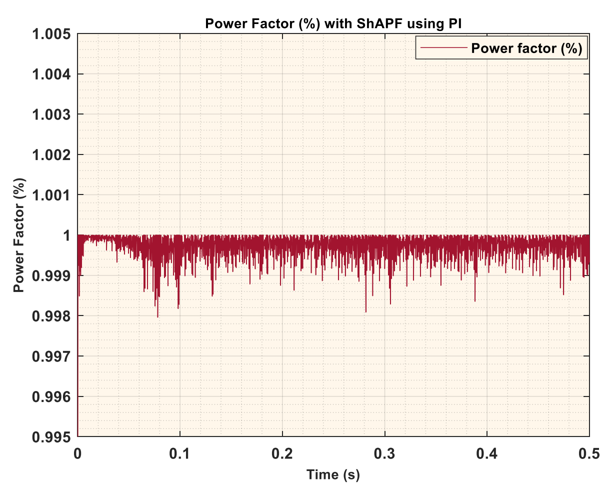

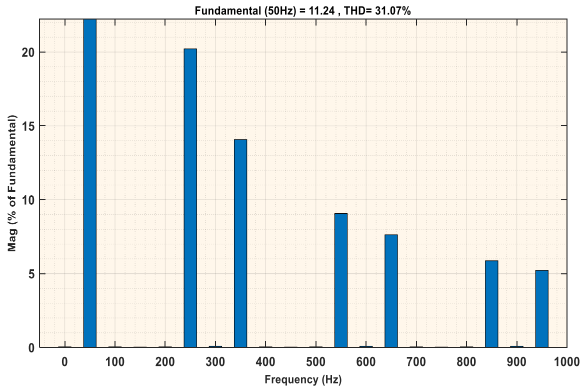

(d) THD.

Figure 15: Without using ShAPF.

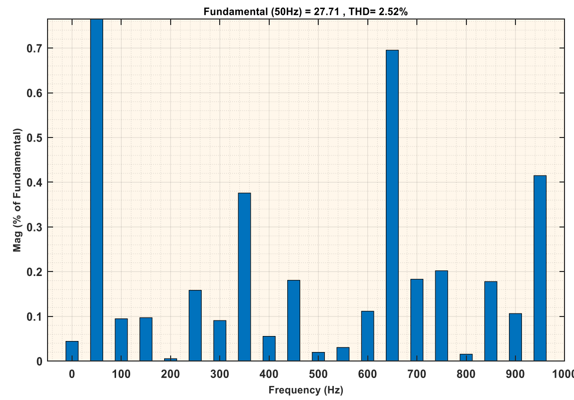

(d) THD.

Figure 16: With using ShAPF-PI.

6.2 Post-filtering

To verify the efficacy of the proposed HNF-ISMC strategy detailed in this paper, this section presents the results of numerical simulations conducted using the PV-UPQC. Simulation outcomes of the system, employing PI controller, classical SMC, and the HNF-ISMC strategy, are provided for three reference currents and DC bus voltage control techniques, with the inclusion of nonlinear loads, as depicted in Figures 16, 17, and 18. These figures elucidate the source current, load current, current generated by the ShAPF (filter current), active and reactive power, power factor, and the total harmonic distortion (THD) for all strategies.

The primary objective of achieving a sinusoidal source current is effectively realized with all techniques employing GWO optimization. These techniques efficiently attenuate the harmonics produced by nonlinear loads and enhance the power factor by reducing reactive power consumption. However, it's essential to note that inadequate regulation of the PI controller and the presence of chattering effects in classical SMC can detrimentally impact energy quality. To address these issues and further improve energy quality, the ShAPF (Shunt Active Power Filter) plays a pivotal role. It absorbs harmonics generated by nonlinear loads at the Point of Common Coupling, resulting in a sinusoidal source current. This improvement is achieved by integrating HNF-ISMC into the control strategy. This observation holds true across all control strategies, as depicted in Figures 16 (a), 17 (a), and 18 (a). By incorporating the ShAPF with HNF-ISMC, the system effectively mitigates harmonic distortion and enhances power quality, ensuring optimal performance and efficiency in power distribution systems.

Furthermore, the ShAPF significantly contributes to reducing reactive power consumption, as depicted in Figures 16 (b), 17 (b), and 18 (b), where the imaginary power approaches zero, indicating a power factor close to unity. Noticeable enhancements are evident in the HNF-ISMC technique. Additionally, it improves the power factor (refer to Figures 16 (c), 17 (c), and 18 (c)), aligning the current with the voltage. HNF-ISMC demonstrates superior performance in achieving a power factor ranging from 0.998 to 1, compared to other techniques such as PI (PF=0.9 to 1) and classical SMC (PF=0.95 to 1). Moreover, Figures 16 (d), 17 (d), and 18 (d) present the total harmonic distortion (THD) of the first-phase source current, with THD values measured at 2.9% for the PI controller, 2.57% for classical SMC, and notably reduced to 1.9% for HNF-ISMC. The THD of the source current remains below 5%, meeting the IEEE-519 standard specifications across all strategies. These results highlight a significant enhancement in power quality with the implementation of the HNF-ISMC strategy alongside the ShAPF. Hence, the integration of the ShAPF with the proposed controller optimized using GWO aims to improve power quality and mitigate harmonic currents.

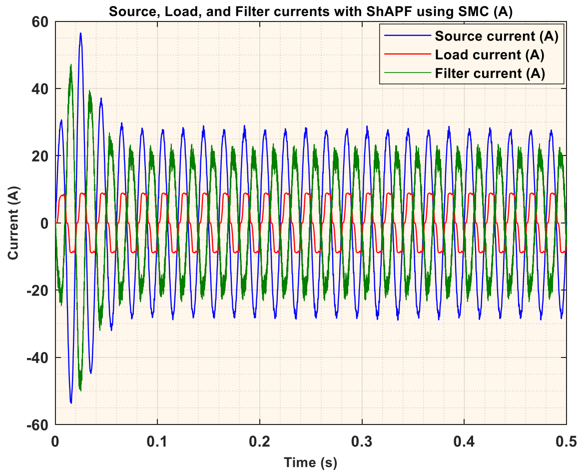

(a) Source, and load, filter currents.

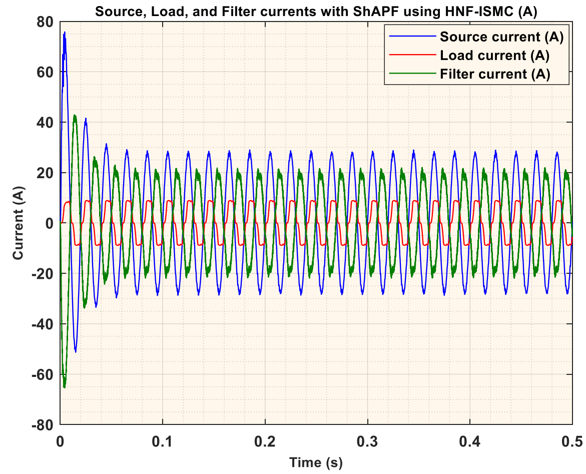

(a) Source, and load, filter currents.

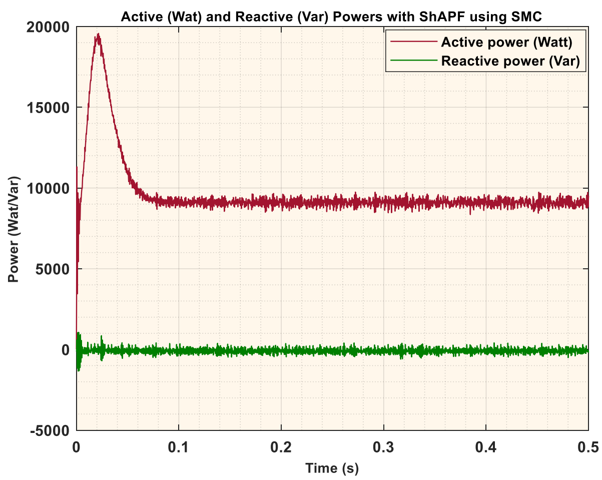

(b) Active, and reactive powers.

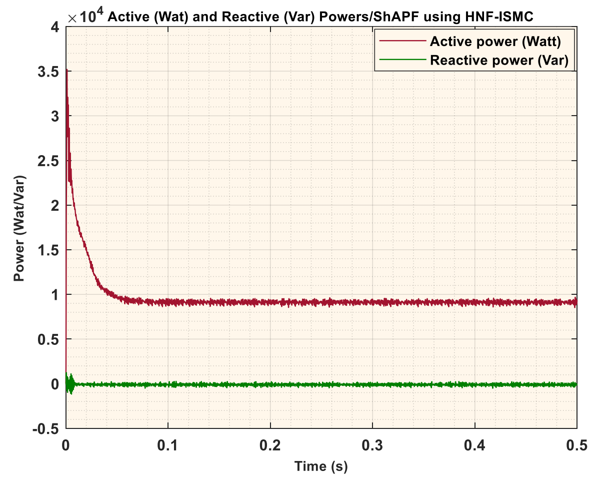

(b) Active, and reactive powers.

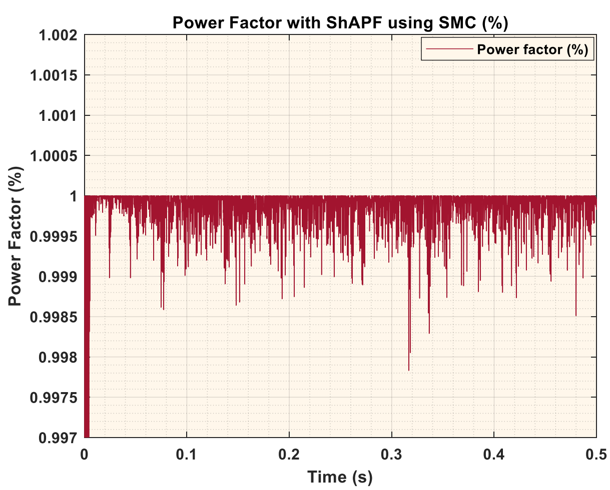

(c) Power factor.

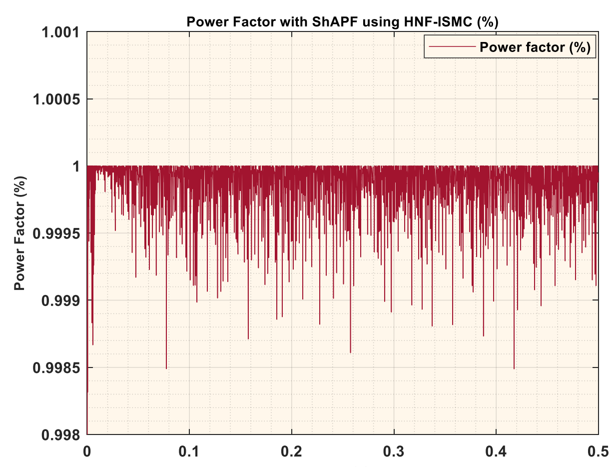

(c) Power factor.

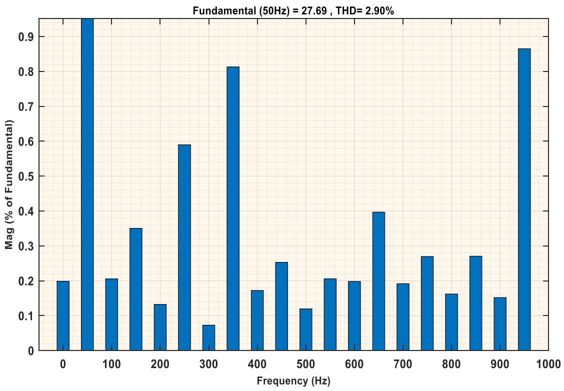

(d) THD.

Figure 17: With using ShAPF-SMC.

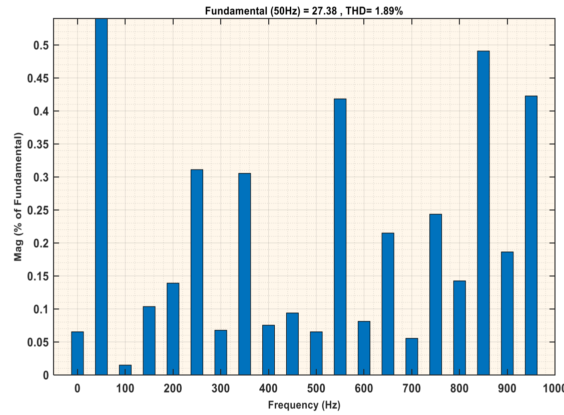

(d) THD.

Figure 18: With using ShAPF- HNF-ISMC.

In Figure 19, the DC-bus voltage is shown reaching its target value of 850 V, starting from an initial value of 830 V, in alignment with the MPPT of the solar PV array. The Hybrid Neuro-Fuzzy Integral Sliding Mode Controller (HNF-ISMC) demonstrates rapid control capabilities, a key feature that distinguishes it from traditional fuzzy logic strategies, especially during system startup. In Figure 19, the HNF-ISMC achieves a settling time of 0.02 s, outperforming the classical sliding mode controller (SMC) with a settling time of 0.03 s, and the PI controller, which takes 0.05 s, under similar operating conditions. When using the PI controller, a deviation of 4 V is observed between 0.02 s to 0.1 s, followed by a 1 V deviation between 1.02 s to 1.08 s, before the voltage stabilizes at 850 V. In contrast, both the classical SMC and HNF-ISMC controllers exhibit no deviation in the voltage. Upon initiation of the ShAPF, the DC-bus voltage decreases by 2 V with the PI controller and classical SMC, while with HNF-ISMC, the decrease is a mere 0.1 V, occurring almost immediately after the ShAPF is connected to the grid. Moreover, HNF-ISMC displays superior performance, characterized by a shorter response time and reduced overshoot, compared to the conventional techniques. This enhanced performance highlights the HNF-ISMC's effectiveness in achieving precise voltage regulation and a faster, more stable response in real-world conditions.

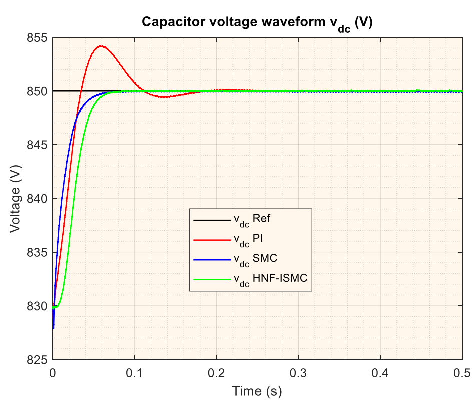

Figure 19: DC-bus voltage waveform.

7 Conclusions

The application of the HNF-ISMC strategy, augmented by the Grey Wolf Optimizer (GWO) for parameter optimization, in Photovoltaic-Unified Power Quality Conditioner (PV-UPQC) systems, particularly in the context of real environmental conditions such as irradiation and temperature in Adrar, Algeria, yields significant advancements in power quality enhancement. By effectively mitigating harmonic currents and compensating reactive power, the HNF-ISMC approach addresses key challenges encountered in grid integration. Moreover, the strategy demonstrates superiority over traditional techniques such as PI and classical SMC, evident in simulations conducted under various scenarios. Notably, the replacement of the discontinuous part of classical SMC mitigates chattering effects, enhancing system stability and performance. Additionally, the utilization of the Shunt Active Power Filter (ShAPF) further contributes to power quality improvement by reducing harmonics and improving the power factor. Overall, the results underscore the efficacy of the HNF-ISMC approach in achieving precise control and mitigating power quality issues in PV-UPQC systems, positioning it as a promising solution for modern grid integration challenges.

Declarations

Conflicts of interests The authors have no competing interests to declare that are relevant to the content of this article.

References

[1] A. Amirullah, A. Ananda, O. Penangsang, A. Soeprijanto, *Load active power transfer enhancement using UPQC-PV-BES system with fuzzy logic controller*, International Journal of Intelligent Engineering and Systems, **13**(2) (2020), 329-349. http://eprints.ubhara.ac.id/id/eprint/1315

[2] M. T. Benchouia, I. Ghadbane, A. Golea, K. Srairi, M. H. Benbouzid, *Design and implementation of sliding mode and PI controllers-based control for three phase shunt active power filter*, Energy Procedia, **50** (2014), 504-511. https://doi.org/10.1016/j.egypro.2014.06.061

[3] S. L. K. Bharathi, S. Selvaperumal, *MGWO-PI controller for enhanced power flow compensation using unified power quality conditioner in wind turbine squirrel cage induction generator*, Microprocessors and Microsystems, **76** (2020), 103080, 1-8. https://doi.org/10.1016/j.micpro.2020.103080

[4] A. Chebabhi, M. K. Fellah, A. Kessal, M. F. Benkhoris, *Comparative study of reference currents and DC bus voltage control for Three-Phase Four-Wire Four-Leg SAPF to compensate harmonics and reactive power with 3D SVM*, ISA Transactions, **57** (2015), 360-372. https://doi.org/10.1016/j.isatra.2015.01.011

[5] Y. Chu, J. Fei, S. Hou, *Dynamic global proportional integral derivative sliding mode control using radial basis function neural compensator for three-phase active power filter*, Transactions of the Institute of Measurement and Control, **40**(12) (2018), 3549-3559. https://doi.org/10.1177/0142331217726955

[6] Y. Chu, S. Hou, J. Fei, *Continuous terminal sliding mode control using novel fuzzy neural network for active power filter*, Control Engineering Practice, **109** (2021), 104735, 1-10. https://doi.org/10.1016/j.conengprac.2021.104735

[7] B. Deffaf, F. Hamoudi, N. Debdouche, *Sliding mode control of a shunt active filter-comparative analysis with conventional PI control*, In 2022 19th International Multi-Conference on Systems, Signals and Devices (SSD), (2022), 1422-1427. http://doi.org/10.1109/SSD54932.2022.9955725

[8] S. Devassy, B. Singh, *Design and performance analysis of three-phase solar PV integrated UPQC*, IEEE Transactions on Industry Applications, **54**(1) (2017), 73-81. http://doi.org/10.1109/TIA.2017.2754983

[9] L. Djilali, A. Badillo-Olvera, Y. Rios, H. López-Beltrán, L. Saihi, *Neural high order sliding mode control for doubly fed induction generator-based wind turbines*, IEEE Latin America Transactions, **20**(2) (2021), 223-232. https://doi.org/10.1109/TLA.2022.9661461

[10] P. Dutta, S. K. Nayak, *Grey wolf optimizer based PID controller for speed control of BLDC motor*, Journal of Electrical Engineering and Technology, **16** (2021), 955-961. https://doi.org/10.1007/s42835-021-00660-5

[11] M. Fodil, A. Djerioui, M. Ladjal, A. Saim, F. Berrabah, H. Mekki, et. al, *Optimization of PI controller parameters by GWO algorithm for five-phase asynchronous motor*, Energies, **16**(10) (2023), 4251, 1-14. https://doi.org/10.3390/en16104251

[12] S. M. Hosseini, M. Manthouri, *Type 2 adaptive fuzzy control approach applied to variable speed DFIG based wind turbines with MPPT algorithm*, Iranian Journal of Fuzzy Systems, **19**(1) (2022), 31-45. https://doi.org/10.22111/IJFS.2022.6549

[13] S. Inthiyaz, R. Nalli, T. Rakesh, K. Subbarao, S. H. Ahammad, V. Rajesh, *GA based PID controller: Design and optimization*, In 2021 6th International Conference on Inventive Computation Technologies (ICICT), (2021), 285-289. http://doi.org/10.1109/ICICT50816.2021.9358640

[14] G. Isha, P. Jagatheeswari, *Optimal allocation of DSTATCOM and PV array in distribution system employing fuzzy-lightning search algorithm*, Automatika, **62**(3-4) (2021), 339-352. https://doi.org/10.1080/00051144.2021.1963080

[15] R. Kumar, *Fuzzy particle swarm optimization control algorithm implementation in photovoltaic integrated shunt active power filter for power quality improvement using hardware-in-the-loop*, Sustainable Energy Technologies and Assessments, **50** (2022), 101820, 1-12. https://doi.org/10.1016/j.seta.2021.101820

[16] S. Lakhdar, F. Ferroudji, K. Roummani, K. Koussa, *Enhanced sensor-less control of DFIG-based generators using hybrid MRAS-ANN observer and PSO parameter optimization*, In 2023 14th International Renewable Energy Congress (IREC), (2023), 1-6. https://doi.org/10.1109/IREC59750.2023.10389203

[17] M. Mirzaee, R. Kazemi, *Type-II fuzzy inference system-based fractional terminal sliding mode control for zero-force exoskeleton robots*, Iranian Journal of Fuzzy Systems, **21**(6) (2024), 147-171. https://doi.org/10.22111/ijfs.2025.49399.8718

[18] M. Mirzaee, A. Nazemi, *Parallel synchronization and a RBF neuro-fuzzy system to synchronization of chaotic systems*, Iranian Journal of Fuzzy Systems, **21**(6) (2024), 101-126. https://doi.org/10.22111/ijfs.2025.48808.8609

[19] A. Moghassemi, S. Padmanaban, V. K. Ramachandaramurthy, M. Mitolo, M. Benbouzid, *A novel solar photovoltaic fed TransZSI-DVR for power quality improvement of grid-connected PV systems*, IEEE Access, **9** (2020), 7263-7279. http://doi.org/10.1109/ACCESS.2020.3048022

[20] J. Morales, L. G. de Vicuna, R. Guzman, M. Castilla, J. Miret, *Modeling and sliding mode control for three-phase active power filters using the vector operation technique*, IEEE Transactions on Industrial Electronics, **65**(9) (2018), 6828-6838. https://doi.org/10.1109/TIE.2018.2795528

[21] I. Oulimar, K. Bouchouicha, N. Bailek, M. Bellaoui, *Statistical study of global solar radiation in the Algerian desert: A case study of Adrar town*, Theoretical and Applied Climatology, **155**(4) (2024), 3493-3504. http://doi.org/10.1007/s00704-024-04834-9

[22] N. Paliwal, L. Srivastava, M. Pandit, *Application of grey wolf optimization algorithm for load frequency control in multi-source single area power system*, Evolutionary Intelligence, **15** (2022), 563-584. https://doi.org/10.1007/s12065-020-00530-5

[23] M. Pichan, M. Mohammadian, *Modelling and digital-based direct power control of shunt active power filter for rectifier loads*, Journal of Modeling in Engineering, **21**(72) (2023), 99-109. https://doi.org/10.22075/JME.2022.26912.2258

[24] L. Saihi, B. Berbaoui, *Mitigation of low voltage electrical network pollution using a two-level PAPF controlled by the ANN-PQ algorithm*, In 2023 International Conference on Electrical Engineering and Advanced Technology (ICEEAT), **1** (2023), 1-5. https://doi.org/10.1109/ICEEAT60471.2023.10425819

[25] L. Saihi, B. Berbaoui, Y. Bakou, *Sliding mode of second-order control based on super-twisting ANFIS algorithm of doubly fed induction generator in wind turbines systems with real variable speeds*, Iranian Journal of Science and Technology, Transactions of Electrical Engineering, **47**(2) (2023), 473-490. https://doi.org/10.1007/s40998-022-00576-4

[26] L. Saihi, B. Berbaoui, H. Glaoui, L. Djilali, S. Abdeldjalil, *Robust sliding mode H∞ controller of DFIG based on variable speed wind energy conversion system*, Periodica Polytechnica Electrical Engineering and Computer Science, **64**(1) (2020), 53-63. http://mjee.iaumajlesi.ac.ir/index/index.php/ee/article/view/2981

[27] L. Saihi, F. Ferroudji, K. Roummani, K. Koussa, Y. Bakou, B. Berbaoui, *Improved harmonic mitigation with a SAP filter connected to a renewable energy source using a novel ANN algorithm*, In 2023 Second International Conference on Energy Transition and Security (ICETS), (2023), 1-6. https://doi.org/10.1109/ICETS60996.2023.10410755

[28] E. Samavati, H. R. Mohammadi, *Active harmonic compensation and stability improvement in high-power grid-connected inverters using unified power quality conditioner*, International Journal of Industrial Electronics Control and Optimization, **6**(3) (2023), 193-204. https://doi.org/10.22111/ieco.2023.45861.1487

[29] K. Sozanski, P. Szczesniak, *Advanced control algorithm for three-phase shunt active power filter using sliding DFT* Energies, **16**(3) (2023), 1453, 1-17. https://doi.org/10.3390/en16031453

[30] R. Thangella, S. R. Yarlagadda, J. Sanam, *Optimal power quality improvement in a hybrid fuzzy-sliding mode MPPT control-based solar PV and BESS with UPQC*, International Journal of Dynamics and Control, **11**(4) (2023), 1823-1843. https://doi.org/10.1007/s40435-022-01095-0

[31] H. Usman, N. Magaji, *Simulation of shunt active power filter based fuzzy logic controller for minimization of total harmonic distortion*, International Journal of Applied and Advanced Engineering Research, **2**(1) (2023), 1-14. https://mediterraneanpublications.com/mejaaer/article/view/172

[32] S. Yamparala, L. Lakshminarasimman, G. S. Rao, *Optimal design of fopid controller for DFIG based wind energy conversion system using grey-wolf optimization algorithm*, International Journal of Renewable Energy Research (IJRER), **12**(4) (2022), 2111-2120. https://doi.org/10.20508/ijrer.v12i4.13446.g8594